



On accretion discs formed in MHD simulations of black hole–neutron star mergers with accurate microphysics

Elias R. Most^{1,2,3}★ L. Jens Papenfort,⁴ Samuel D. Tootle⁴ and Luciano Rezzolla^{4,5,6}

¹Princeton Center for Theoretical Science, Princeton University, Princeton, NJ 08544, USA

²Princeton Gravity Initiative, Princeton University, Princeton, NJ 08544, USA

³School of Natural Sciences, Institute for Advanced Study, Princeton, NJ 08540, USA

⁴Institut für Theoretische Physik, Goethe Universität, Max-von-Laue-Str. 1, D-60438 Frankfurt am Main, Germany

⁵School of Mathematics, Trinity College, Dublin 2, Ireland

⁶Frankfurt Institute for Advanced Studies, Ruth-Moufang-Str. 1, D-60438 Frankfurt am Main, Germany

Accepted 2021 June 14. Received 2021 June 12; in original form 2021 May 12

Downloaded from <https://academic.oup.com/mnras/article/506/3/3511/6312506> by UNAM user on 01 March 2024

ABSTRACT

Remnant accretion discs formed in compact object mergers are an important ingredient in the understanding of electromagnetic afterglows of multimessenger gravitational-wave events. Due to magnetically and neutrino-driven winds, a significant fraction of the disc mass will eventually become unbound and undergo r-process nucleosynthesis. While this process has been studied in some detail, previous studies have typically used approximate initial conditions for the accretion discs, or started from purely hydrodynamical simulations. In this work, we analyse the properties of accretion discs formed from near equal-mass black hole–neutron star mergers simulated in general-relativistic magnetohydrodynamics in dynamical spacetimes with an accurate microphysical description. The post-merger systems were evolved until 120 ms for different finite-temperature equations of state and black hole spins. We present a detailed analysis of the fluid properties and of the magnetic-field topology. In particular, we provide analytic fits of the magnetic-field strength and specific entropy as a function of the rest-mass density, which can be used for the construction of equilibrium disc models. Finally, we evolve one of the systems for a total of 350 ms after merger and study the prospect for eventual jet launching. While our simulations do not reach this stage, we find clear evidence of continued funnel magnetization and clearing, a prerequisite for any jet-launching mechanism.

Key words: accretion disc – stars: neutron – MHD – black hole - neutron star mergers.

1 INTRODUCTION

Recently, LIGO has announced early results of the third observing run, indicating the potential detection of several black hole (BH)–neutron star (NS) systems. Two of them, S200105ae and S200115j, have recently been studied by optical follow-up observations (Anand et al. 2021), albeit no kilonova afterglow has so far been detected. Since the kilonova of these systems would be mainly driven by secular disc mass ejecta, a potential non-detection can set tight constraints on the allowed range of parameters. In particular, retaining a sufficient disc mass after the merger of a small mass-ratio system also requires high BH spin (Foucart, Hinderer & Nissanka 2018). Therefore, a non-detection in conjunction with the inferred binary parameters from the inspiral allows us to probe the BH spin (Anand et al. 2021; Raaijmakers et al. 2021), and for low-mass BHs also the equation of state (EOS) (Fragione & Loeb 2021). Several works have also further investigated the prospects for constraining the EOS with BH–NS gravitational-wave events (e.g. Pannarale et al. 2011a; Maselli, Gualtieri & Ferrari 2013; Lackey et al. 2014). While an initial estimate of the amount of mass ejection can easily be done, a more accurate calculation requires more precise knowledge of the

amount of unbound disc mass, its nuclear composition, velocity, and temperature distributions. In turn, this necessitates a careful investigation of the initial accretion discs from which these mass outflows originate.

The merger and early post-merger of BH–NS systems have been explored in great detail, placing an emphasis on the disc formation, mass ejection, and gravitational-wave emission (Shibata & Uryū 2006; Shibata & Uryū 2007; Liu et al. 2008; Shibata & Taniguchi 2008; Etienne et al. 2009; Kyutoku, Shibata & Taniguchi 2010; Foucart et al. 2011; Kyutoku et al. 2011; Pannarale, Tonita & Rezzolla 2011b; Foucart 2012; Foucart et al. 2012, 2013b; Kyutoku et al. 2015). Whereas those simulations have focused on quasi-circular binaries most relevant for gravitational-wave detections, some simulations have also investigated the merger of eccentric encounters (East, Paschalidis & Pretorius 2015). More recent studies have also included finite-temperature equations of state and neutrino transport (Foucart et al. 2013a, 2014, 2015, 2017; Kyutoku et al. 2018), allowing them to investigate the nuclear composition of the mass ejecta. Based on such numerical simulations, it has also been possible to accurately predict the masses of the discs formed in these mergers (Foucart 2012; Foucart et al. 2018). Although simulations have mainly been performed for mass ratios $q := m_2/m_1 < 1/4$ – where $m_{1,2}$ are the masses of the binary components – a few studies have been conducted for systems in the near equal-mass regime (Foucart

* E-mail: emost@princeton.edu

et al. 2019; Hinderer et al. 2019; Hayashi et al. 2021), which is also the focus of this work. The formation channels for such near-equal mass systems are still a topic of active research (Drozda et al. 2020; Zevin et al. 2020). While some of the remnant accretion discs formed in all of these simulations have been studied with superimposed magnetic fields to understand their long-term evolution (Fernández et al. 2017; Nouri et al. 2018; see also Lee & Ramirez-Ruiz 2002; Belczynski et al. 2008), relatively few general-relativistic BH–NS merger simulations with magnetic fields initially confined to the NS have been conducted. Practically all of them have used polytropic equations of state (Chawla et al. 2010; Etienne et al. 2012b; Etienne, Paschalidis & Shapiro 2012c; Kiuchi et al. 2015; Paschalidis, Ruiz & Shapiro 2015; Wan 2017; Ruiz, Shapiro & Tsokaros 2018b). To the best of our knowledge, this work presents the first study to self-consistently investigate the merger and post-merger of BH–NS systems with initial NS magnetic fields, finite-temperature equations of state, and neutrino leakage, where the latter has been found to reasonably approximate the evolution of the nuclear composition in the cold ($T < 10$ MeV) accretion discs present in these systems (Kyutoku et al. 2018).

More specifically, we study the post-merger formation of an accretion disc in nearly equal-mass BH–NS mergers for two finite-temperature EOS and a magnetic field initially confined to the NS. The early post-merger evolution and mass ejection of these systems has been presented in Most et al. (2020a). The follow-up simulations presented here highlight the early magnetic field and composition evolution until ~ 120 ms, and provide a detailed account of the properties of the accretion disc formed in the merger and along its subsequent evolution. Finally, we evolve one of the configurations for up to 350 ms and comment on the prospects of jet launching from such systems, which would make them suitable for the production of short gamma-ray bursts (Lee & Ramirez-Ruiz 2007).

2 METHODS

In this section, we provide a short overview of numerical methods and the initial conditions used in this study.

We model the initial BH–NS systems as having irrotational NSs and spinning BHs on quasi-circular orbits (Grandclément 2006; Papenfort et al. 2021). The initial models are valid solutions of the constraint sector of the Einstein equations constructed using the conformally flat XCTS formalism. The excision boundary conditions on the BH include a Neumann boundary condition on the lapse and a tangential shift condition to control the quasi-local spin of the BH (Caudill et al. 2006). The interior of the BH is initially regularized by extrapolating the solution using an eighth-order Lagrangian polynomial along the radial direction (Etienne et al. 2007; Etienne et al. 2009). The NS is described by either of two EOSs, TNTYST (Togashi et al. 2017) or BHBA Λ Φ (Banik, Hempel & Bandyopadhyay 2014) in line with multimessenger constraints on the NS maximum mass (Margalit & Metzger 2017; Rezzolla, Most & Weih 2018; Ruiz, Shapiro & Tsokaros 2018a; Shibata et al. 2019; Nathanail, Most & Rezzolla 2021) and radius (Abbott et al. 2018; Annala et al. 2018; De et al. 2018; Most et al. 2018; Raithel, Özel & Psaltis 2018). The initial NSs are endowed with an internal dipole field via the vector potential $A_\phi = \varpi^2 A_0 \max(p - 0.04 p_{\max}, 0)^2$, commonly used in these types of simulations (Liu et al. 2008; Giacomazzo, Rezzolla & Baiotti 2011; Etienne et al. 2012b; Kiuchi et al. 2015), where p_{\max} refers to the maximum pressure in the NS. The coefficient, A_0 , is chosen such that the maximum field strength in the centre of the star corresponds to $\simeq 10^{14}$ G. A summary of the initial conditions is given in Table 1.

In general, it is both interesting and important to understand the behaviour of a variety of discs in terms of disc masses, compositions, and magnetic-field topologies, in order to get a good coverage of the large parameter space. Since we are interested in studying near equal-mass systems consistent also with very massive NS binaries, we focus on systems along the stability line (in terms of spins χ) of the most massive NSs (Most, Weih & Rezzolla 2020b), as presented in Most et al. (2020a). This assumption correlates the BH mass M_{BH} with the BH spin χ_{BH} , leading to a parametrization only dependent on the maximum mass M_{TOV} of a non-rotating NS (Most et al. 2020b). More details on this construction can be found in Most et al. (2020b).

2.1 Numerical methods

In order to model the dynamical evolution of the BH–NS system, we solve the general-relativistic ideal magnetohydrodynamics (GRMHD) equations together with the Einstein field equations (EFE)

$$\nabla_\mu T^{\mu\nu} = -Q^\nu, \quad (1)$$

$$R_{\mu\nu} = 8\pi \left(T_{\mu\nu} - \frac{1}{2} g_{\lambda\kappa} T^{\kappa\lambda} g_{\mu\nu} \right) + 2\nabla_{(\mu} Z_{\nu)} + \kappa_1 [2n_{(\mu} Z_{\nu)} - n_\alpha Z^\alpha g_{\mu\nu}], \quad (2)$$

where $g_{\mu\nu}$ is the 4D Lorentzian space–time metric, $R_{\mu\nu}$ the corresponding Ricci tensor, and $T_{\mu\nu}$ the energy momentum tensor describing the NS matter and the magnetic fields.

The source term Q^ν represents the energy and momentum loss due to weak interactions. Using the unit normal vector n_μ of the 3+1 slicing of the space–time (Gourgoulhon 2012) and the Z-vector Z_μ within the Z4 system (Bona et al. 2003), the EFE are written as a system that allows for the propagation of numerical constraint violations of the Einstein system (Gundlach et al. 2005). We solve the EFE using the Z4c formulation (Bernuzzi & Hilditch 2010; Hilditch 2013), which is a conformal variant of the Z4 system (Bona et al. 2003) (see also Alic et al. 2012). Different from Weyhausen, Bernuzzi & Hilditch (2012), we find that simulations of BH–NS binaries employing the excision formalism on the initial data require additional damping, $\kappa_1 = 0.07$, whereas larger damping leads to instabilities of the space–time evolution. In addition, we find it beneficial to remove the advection part in the shift condition, which is then given by (Alcubierre et al. 2003; Etienne et al. 2008),

$$\partial_t \beta^i = B^i, \quad (3)$$

$$\partial_t B^i = \frac{3}{4} \bar{\Gamma}^i - \eta B^i, \quad (4)$$

with damping parameter $\eta = 1.4$.

The ideal-GRMHD equations (Duez et al. 2005; Shibata & Sekiguchi 2005; Giacomazzo & Rezzolla 2007) are supplemented by an evolution equation for the magnetic vector potential in the ideal-MHD limit (Del Zanna, Bucciantini & Londrillo 2003; Etienne, Liu & Shapiro 2010). We additionally impose the Lorenz gauge for the vector potential (Etienne et al. 2012a). Neutrino losses are incorporated using a simplified leakage prescription (Ruffert, Janka & Schaefer 1996; Rosswog & Liebendörfer 2003; Galeazzi et al. 2013), that is appropriate for the low temperatures reached in the tidal disruption of an NS (Deaton et al. 2013; Kyutoku et al. 2018).

These equations are solved using the Frankfurt/IllinoisGRMHD code (FIL) (Most et al. 2019a; Most, Papenfort & Rezzolla 2019b). Although FIL is derived from the IllinoisGRMHD code (Etienne et al. 2015), it makes use

Table 1. Summary of the properties of the initial binaries. The columns list: the gravitational component masses in isolation, m_{BH} and m_{NS} , the baryon mass m_b of the secondary, the mass ratio $q = m_{\text{NS}}/m_{\text{BH}}$, the dimensionless spin χ_{BH} of the BH (primary), the effective spin $\tilde{\chi} := \chi_1/(1+q)$ of the binary, and the EOS describing the nuclear matter. All binaries have a total mass $M_{\text{ADM}} = 3.6 M_{\odot}$ and are at an initial separation of 45 km. The NS (secondary) is always non-rotating, $\chi_{\text{NS}} = 0$. We also state the final, post-merger BH spins $\chi_{\text{BH}}^{\text{fin}}$ and disc masses M_b^{fin} first reported in Most et al. (2020a).

	$m_{\text{BH}} (M_{\odot})$	$m_{\text{NS}} (M_{\odot})$	$m_b (M_{\odot})$	q	χ_{BH}	$\tilde{\chi}$	$M_b^{\text{fin}} [M_{\odot}]$	$\chi_{\text{BH}}^{\text{fin}}$	EOS
TNT.chit.0.00	2.20	1.40	1.55	0.636	0.00	0.00	0.013	0.73	TNTYST
TNT.chit.0.15	2.24	1.36	1.50	0.608	0.24	0.15	0.057	0.79	TNTYST
TNT.chit.0.35	2.42	1.18	1.28	0.486	0.52	0.35	0.170	0.83	TNTYST
BHBLP.BH.chit.0.00	2.10	1.50	1.65	0.636	0.00	0.00	0.033	0.77	BHBΛΦ
BHBLP.BH.chit.0.15	2.14	1.46	1.60	0.608	0.24	0.15	0.073	0.82	BHBΛΦ
BHBLP.BH.chit.0.35	2.33	1.27	1.37	0.543	0.54	0.35	0.124	0.86	BHBΛΦ

of a fully fourth-order conservative finite-difference algorithm to discretize the hydrodynamical and electromagnetic flux terms (Del Zanna et al. 2007). Furthermore, it provides routines to use tabulated finite-temperature EOSs and can evolve the electron fraction Y_e . In addition, FIL solves the Z4c system using fourth-order accurate upwinded finite-differences (Zlochower et al. 2005). Details on the implementation and accuracy of the code can be found in Most et al. (2019b).

FIL is built on top of the Einstein Toolkit (Loeffler et al. 2012; Babiuc-Hamilton et al. 2019). As such, FIL uses a fixed-mesh box-in-box refinement provided by Carpet (Schnetter, Hawley & Hawke 2004). Specifically, we use nine nested Cartesian boxes each at doubling resolution. The outer domain extends to $\simeq 6000$ km in each direction and the initial compact objects are covered by the two finest domains with a size of 17.7 km and a resolution of $\simeq 215$ m. Additionally, we impose reflection symmetry along the vertical z -direction.

3 RESULTS

In this work, we study the merger and post-merger evolution of near equal-mass BH-NS binaries. Before turning to the properties of the accretion discs formed in such mergers, we first provide a very brief overview of their formation. We do this by considering the fiducial system TNT.chit.0.35. In order to illustrate the disc formation process, we begin by summarizing the dynamical formation of the disc in Fig. 1, which reports the comoving magnetic energy density b^2 , the rest-mass density ρ , the electron fraction Y_e , and the local fluid temperature T . The different rows correspond to meridional (top panels) and equatorial (bottom panels) views of the accretion disc around the BH, while the different columns correspond to different times after the merger. The general dynamics of this process have been studied extensively in purely hydrodynamical simulations (Etienne et al. 2009; Kyutoku et al. 2011; Foucart et al. 2012). In order for a massive disc to form during and after merger, tidal disruption has to occur outside of the innermost stable circular orbit (ISCO) of the BH (Shibata & Taniguchi 2011; Pannarale et al. 2011b). Starting from the left-hand panel, we can see that shortly after tidal disruption, an initial accretion disc begins to form around the BH. Originating from the cold NS matter, the initial disc is very neutron rich ($Y_e < 0.05$), but already reaches temperatures $T \lesssim 10$ MeV. The disc quickly grows in mass and size due to fall-back accretion from the tidal arm (middle column), begins to circularize and a steady accretion flow develops over time. As expected, this happens on the dynamical time-scales of the discs, which are proportional to the disc mass M_{disk}^b , so that the lightest discs circularize first. Initially, the pure neutron matter is far out of beta-equilibrium under these conditions and will rapidly re-equilibrate via beta decay of neutrons, leading to an increasing

protonization especially of the low-density parts of the disc. At the same time, the magnetic-field strength is increasing throughout the disc, exceeding 10^{14} G locally. More details on the magnetic-field evolution will be given in Section 3.3. Finally, after more than 50 ms past merger, the disc has settled into an initial quasi-equilibrium, consisting of a very neutron-rich disc, probing rest-mass densities $\lesssim 10^{11}$ g cm $^{-3}$. A disc formed by this process will then set the initial conditions for the long-term evolution in terms of the accretion flow and mass ejection (Fernández et al. 2015, 2017).

3.1 Disc properties

One of the most important observables of such a gravitational-wave event would be the associated optical counterparts, in particular the kilonova afterglow (see Metzger 2017, for a review). In the case of a BH-NS merger with a massive remnant accretion disc, this will be caused primarily by secular (essentially magnetically and neutrino driven) disc mass ejection (Fernández & Metzger 2013; Fernández et al. 2015; Siegel & Metzger 2017). In addition, dynamical mass ejection will also lead to an early red kilonova component (Foucart et al. 2013b; Kyutoku, Ioka & Shibata 2013; Kyutoku et al. 2015; Kawaguchi et al. 2016). Previous simulations of realistic (e.g. Fernández et al. 2017; Nouri et al. 2018) or idealized (e.g. Siegel & Metzger 2017; Fernández et al. 2019) remnant discs have shown that a large fraction of the disc material will become unbound. Therefore, it is important to understand the initial structure of realistic discs formed during merger by the tidal disruption of the NS.

3.1.1 General observations

In this section, we will focus on the composition of the disc formed after the merger and will highlight part of its evolution. As discussed in the previous section using Fig. 1, the disc is formed by the tidal disruption of the NS at merger. The neutron-rich debris then forms an accretion disc, which will become quasi-stationary once the fall-back accretion of matter from the bound part of the tidal tail has ceased. Generically, we find that this happens after roughly 50 – 70 ms.

Having outlined the general stages of the disc formation process, we now present the resulting discs for three different effective spins $\tilde{\chi} := \chi_1/(1+q) = [0.00, 0.15, 0.35]$ of the binary, performed with both the TNTYST and BHBΛΦ EOS. In Fig. 2 the rest-mass density ρ , electron fraction Y_e , and temperature T are shown on the equatorial plane for the three effective spins at a time $t \approx 100$ ms after merger.

We begin by discussing the evolution of the TNTYST systems (top row), although all conclusions will essentially also hold for the BHBΛΦ EOS, as can be seen from the bottom row of Fig. 2. This is because the smaller compactness $C = M/R$ of the initial

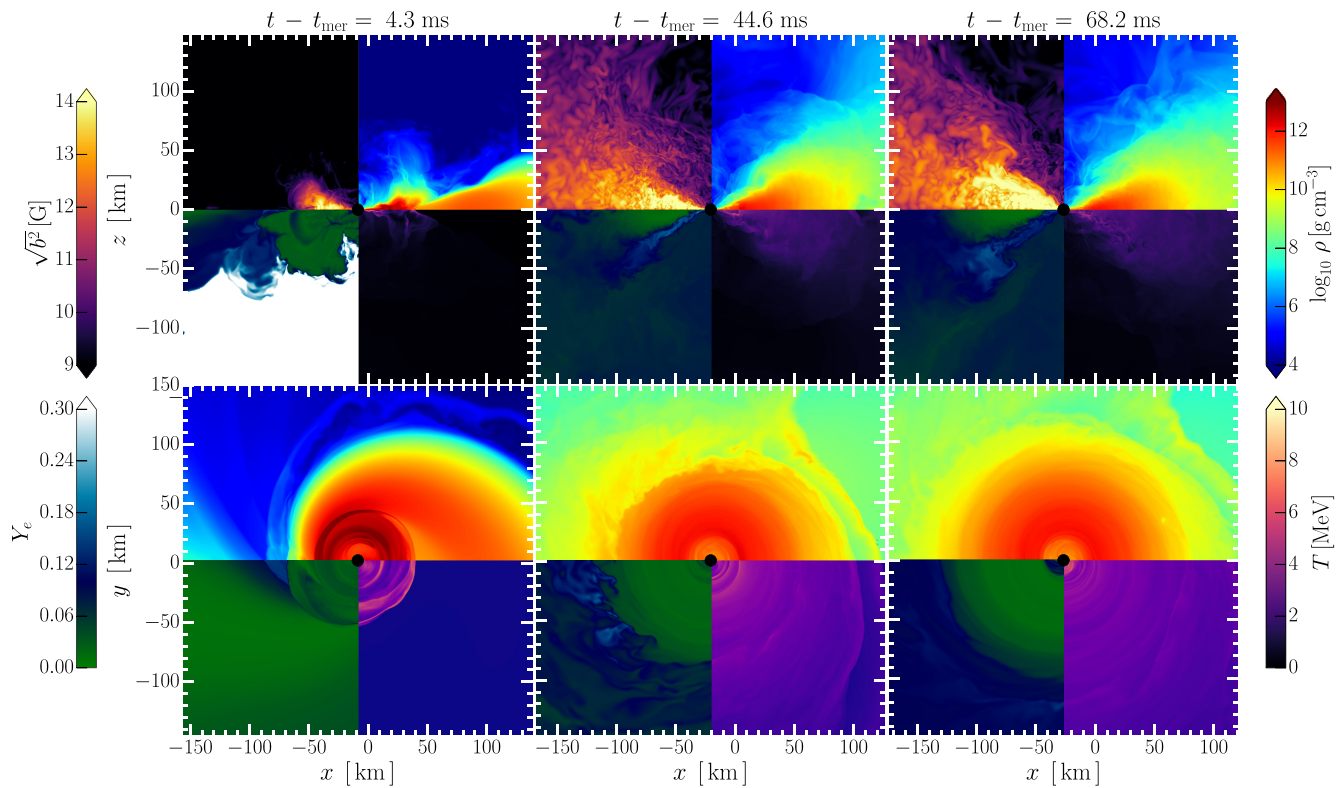


Figure 1. Model TNT.chit.0.35. Shown are the comoving magnetic energy density b^2 , the rest-mass density ρ , the electron fraction Y_e , and the local fluid temperature T . The different rows correspond to meridional (top) and equatorial (bottom) views of the accretion disc around the BH. The columns correspond to different times after merger, starting from the early formation of the disc after the star has been tidally disrupted (left-hand column). The centre and right-hand columns then refer to two times where the disc grows due to fall-back accretion of the bound tidal arm, and the onset of a steady accretion flow. All times are stated relative to the merger time t_{mer} .

NS for the $\text{BHB}\Lambda\Phi$ EOS only leads to an enhancement in the disc mass (Foucart 2012), consistent with the fact that different EOSs will affect mostly the amount of remnant disc mass, but hardly the spin of the BH or the low-density part of the EOS (Timmes & Swesty 2000) probed in the accretion disc. Tidal disruption depends on the mass ratio and spin of the BH (Shibata & Taniguchi 2008) (see also Shibata & Taniguchi (2011) for a review). More precisely, depending on the different effective spins of the BH (and hence also mass ratios), tidal disruption can be enhanced in our set of models (Most et al. 2020a). Indeed, we find that spin enhances the disc mass as expected from previous studies (Foucart et al. 2018), creating the most extended and massive disc for the high-spin system (left-hand panel), with a mass $M_b^{\text{disc}} = 0.17 M_\odot$ (see Table 1). At the same time, the zero-spin system TNT.chit.0.00 only reaches disc masses of $M_b^{\text{disc}} = 0.01 M_\odot$. Interestingly, the intermediate case with effective spin $\tilde{\chi} = 0.15$ features the highest rest-mass densities of all cases. The magnetic-field strength is highest in the high-spin case, and lowest in the case of zero BH spin. A more detailed discussion of the magnetic-field evolution will be given in Section 3.3. The temperature, T , also increases monotonically with spin, albeit in all cases the discs are rather cold $T \lesssim 10 \text{ MeV}$, and cooling over time.

The continued emission of neutrinos leads to a rapid cooling of the disc, which is shown in Fig. 3. Different from the collision of two NSs, where the compression at merger can produce very high temperatures $\gg 10 \text{ MeV}$ (Perego, Bernuzzi & Radice 2019; Endrizzi et al. 2020), tidal disruption is not able to significantly heat up the baryonic matter in the simulation. In fact, when comparing

the different evolutions of the hottest fluid elements in the simulation domain (top panels of Fig. 3), we find that, at most, temperatures of 15 MeV are reached in the case of TNT.chit.0.35 and about 10 MeV in the lower spin cases. Neutrino emission then leads to a rapid cool-down of the disc to below 10 MeV on a time-scale of about ~ 50 ms. The magnitude of neutrino luminosity from the disc is also less for the low-spin models (bottom panels of Fig. 3), consistent with the discs being colder. In all cases the initial neutrino luminosity is at least $10^{50} \text{ erg s}^{-1}$.

We can further see in Fig. 2 that the ‘funnel’ region is mildly polluted with neutron-rich matter, except in the case of low-spin TNTYST models, which feature lower densities at higher electron fraction. This likely indicates that this matter is closer to beta-equilibrium which corresponds to more symmetric matter at those densities.

3.1.2 Nuclear composition and weak interactions

When looking at the nuclear composition of the discs, in terms of the electron fraction Y_e , we can see that the discs become more neutron rich with increasing effective spin. Furthermore, the discs begin to rapidly protonize in the outer layers, since these are transparent to neutrino emission. This can easily be understood when considering that the discs, initially formed from almost pure neutron matter in the tidal disruption process, have a composition that is far from beta-equilibrium under the post-merger conditions. Hence, beta-decay will lead to an increase in the proton–neutron ratio in the disc, that is

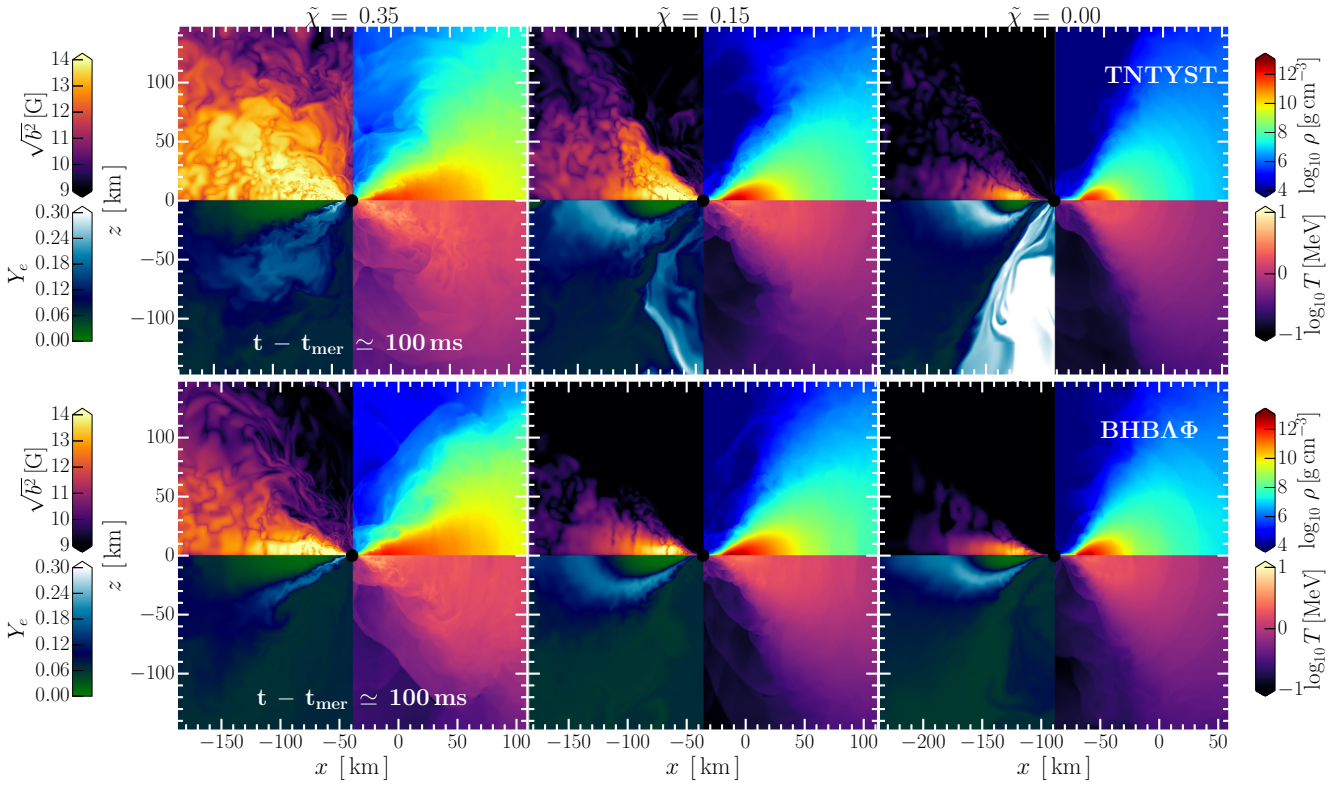


Figure 2. Shown are the evolution of the comoving magnetic energy density b^2 , the rest-mass density ρ , the electron fraction Y_e , and the local fluid temperature T in the meridional plane. The top row shows models computed using the TNTYST EOS, while the bottom row the BHBA Φ EOS. All results are shown at ≈ 100 ms after merger at time t_{mer} .

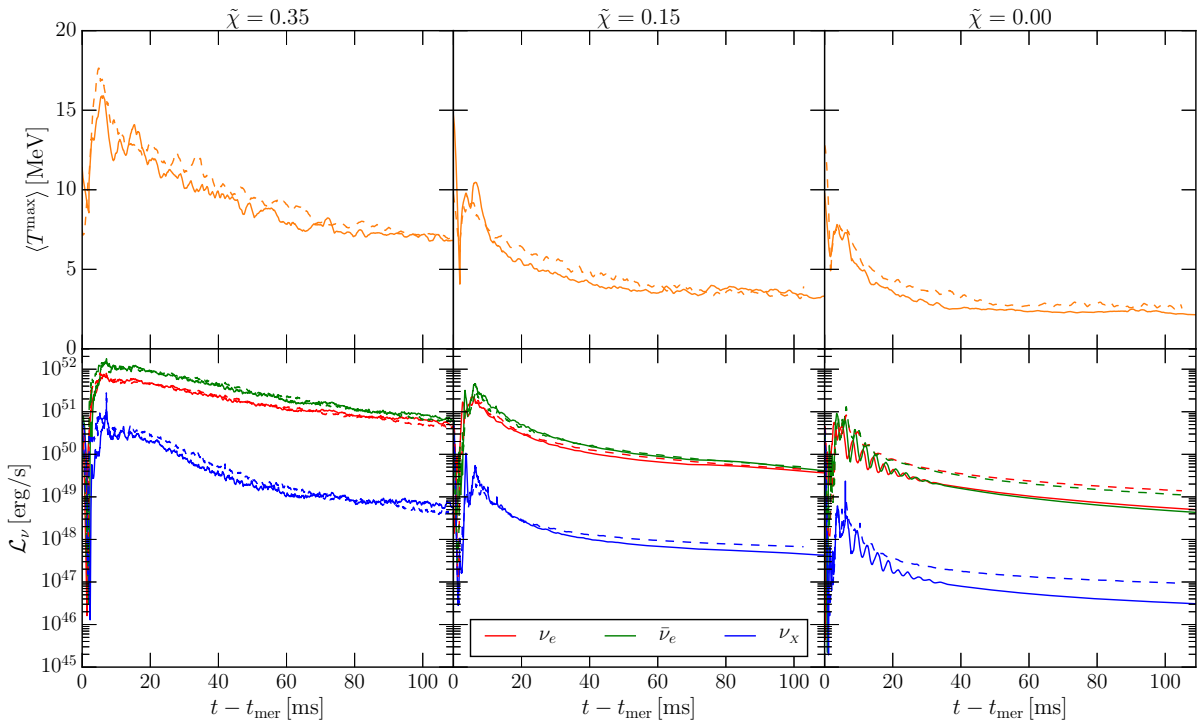


Figure 3. Temperature evolution and neutrino emission of the disc. (Top) time-averaged maximum temperature $\langle T^{\max} \rangle$. (Bottom) neutrino luminosity \mathcal{L}_v . Results are shown for simulations with the TNTYST (solid) and BHBA Φ EOSs. The columns represent the different models in terms of their effective spin $\tilde{\chi}$.

accompanied by an emission of neutrinos. Quantitatively, this leads to an increase in the electron fraction which easily reaches $Y_e \simeq 0.2 - 0.3$. While this is most pronounced for the medium and zero spin cases (right-hand and middle columns in Fig. 2), we expect that on larger time and length scales the disc in the highest spin case (left-hand column) will exhibit a similar behaviour.

This effect has been closely investigated by De & Siegel (2020), who found that starting with constant specific angular momentum and specific entropy disc equilibria, low-mass discs protonize more quickly and that weak interactions switch-off in these discs. Different from these idealized accretion discs, we find that the protonization is not highest in the centre around the BH but largely affects a ring of low-density material. In Fig. 4 the spatial distribution of the specific entropy s and the lepton chemical potential μ_l is reported, for which the latter tends to zero in beta-equilibrium.¹ Indeed, this proton-rich ring quickly beta-equilibrates (blue regions), as $\mu_l/k_B T \ll 1$. Interestingly, we find that in the case of the BHB $\Lambda\Phi$ models (bottom row) an inner ring of matter close to beta-equilibrium develops, whereas the outer ring is less equilibrated than in the TNTYST cases. This inner ring is seemingly absent for models with the TNTYST EOS (top row). Moreover, we find that our realistic remnant accretion discs feature density-dependent variations of the specific entropy, $s < 10$.

To complete our discussion on weak interactions in the disc, we briefly point out the presence of disc self-regulation (Chen & Beloborodov 2007; Siegel & Metzger 2017), following the discussion in Siegel & Metzger (2018). While Fig. 4 would imply that large parts of the disc are out of beta-equilibrium and would have to protonize, self-regulation at the inner edge of the disc, will lead to neutronization that maintains $Y_e \simeq 0.1$. This is because in this neutrino transparent regime copious e^\pm -pair production will effectively modify the beta-equilibrium condition (Beloborodov 2003). The balance between turbulent heating (induced by the magnetorotational instability, see Section 3.3) and neutrino cooling will then establish this reservoir of neutron-rich matter in the inner edge of the disc.

Although this study primarily focuses on obtaining initial conditions for discs after tidal disruption, our long-term simulation (TNT.chit.0.35), was run long enough to exhibit this behaviour. Indeed, as shown in the top panels of Fig. 5, the disc is initially (i.e. at $t - t_{\text{mer}} = 100$ ms) very neutron rich with $Y_e < 0.15$, since it was formed from the neutron-rich matter of the tidal disrupted NS. However, at the final time of our simulation (i.e. at $t - t_{\text{mer}} = 350$ ms), large parts of the disc have already begun to protonize, reaching $Y_e \simeq 0.2$ at larger distances $r > 80$ km from the BH, where densities are larger and the cooling less effective. We can also see this by looking at the temperature profiles in the bottom panels of Fig. 5. More specifically, at later times while the main part of the disc cools only slowly, close to the BH and at distances $r < 40$ km, where the densities are smaller and the cooling is more effective, most of the disc matter is even more neutron rich than initially, i.e. having $Y_e <$

¹We recall that for the conserved quantum numbers charge Q , baryon number B , and lepton number l [e.g. a neutron is a baryon ($B = 1, l = 0$) with zero electric charge ($Q = 0$)], the chemical potential will split as

$$\mu = B\mu_B + Q\mu_Q + l\mu_l,$$

where $\mu_{B,Q,l}$ are the associated chemical potentials. Thus, for beta-equilibrium,

$$\mu_p + \mu_e - \mu_n = \mu_l \rightarrow 0,$$

using the neutron chemical potential, $\mu_n = \mu_B$, the proton chemical potential, $\mu_p = \mu_B + \mu_Q$, and the electron chemical potential $\mu_e = \mu_l - \mu_Q$.

0.1. This is consistent with the onset of self-regulation and broadly agrees with the findings presented in Siegel & Metzger (2018).

3.2 Bulk hydrodynamic properties

We now focus on the hydrodynamic properties of the accretion disc. When constructed as equilibrium configurations in axisymmetry (Fishbone & Moncrief 1976), accretion discs are usually described in terms of the specific angular momenta j , specific entropies s , disc masses M_{disc} , and their electron fractions Y_e . Typically, those are assumed to be constants in most previous studies (e.g. Siegel & Metzger 2017; Fernández *et al.* 2019). Having a set of fully consistent GRMHD simulations of accretion discs formed by tidal disruption in the merger of BH–NS systems, does in fact allow us to compute realistic distributions of the above fluid quantities as functions of the rest-mass density ρ . These are shown in Fig. 6 for simulations using the TNTYST EOS. Starting from the top, we first show the temperature distributions that, in all of the three cases, exhibit a flat plateau around $T \simeq 2$ MeV, which changes to a fall-off for rest-mass densities $\rho < 10^9$ g cm⁻³. The entropy profiles (second row from the top) are almost linear in all cases, starting from specific entropies $s < 1$ at the highest densities and extending outwards until $s \approx 7 - 8$ for the lowest densities in the discs, $\rho \simeq 10^5$ g cm⁻³. Interestingly, low-mass discs, i.e. obtained for $\tilde{\chi} = [0.00, 0.15]$, seem to feature a small plateau around $\rho \simeq 10^9$ g cm⁻³, corresponding roughly to the transition to the nuclear statistical equilibrium EOS used at low densities. Overall, it is possible to provide an effective fit for the specific entropy in terms of the function

$$s = \sum_{k=0}^5 c_k (\log_{10}[\rho / (\text{g cm}^{-3})])^k, \quad (5)$$

where the numerical values for the coefficients c_k are provided in Table 2.

Focussing on the electron fraction Y_e , we can continue our earlier discussion around Fig. 4, where a ring-like structure in the disc approaching beta-equilibrium is observable. Looking at $Y_e(\rho)$ (third row from the top in Fig. 6), we can see that the bulk of the matter in the disc follows a tight relation with the rest-mass density. The innermost, densest parts of the disc, i.e. $\rho > 10^{10}$ g cm⁻³, are at very low electron fractions, $Y_e < 0.05$, thus implying that most of the disc is made of almost pure neutron matter. Moving outwards to lower densities and approaching the beta-equilibrated ring (for $\tilde{\chi} = 0.00, 0.15$), the electron fraction peaks at $Y_e = 0.25$ for densities around $\rho = 10^9$ g cm⁻³. Instead of continuing to increase as would be predicted in beta-equilibrium,² the electron fraction decreases again to below $Y_e < 0.1$. For the highest-spin case, the situation is slightly different. We can see that a small fraction of the disc material exhibits a similar (beta-equilibrated) Y_e -peak as in the other cases, but most of the disc remains at electron fractions $Y_e < 0.1$, indicating that the entire disc remains neutron rich. This is consistent with the weak-interaction ‘ignition threshold’ proposed by De & Siegel (2020).

Concerning the specific angular momentum that governs the structure of the disc (bottom row), we find that depending on the effective spin $\tilde{\chi}$ and, hence, on the disc mass, the distributions look very different. Although there are different definitions of the relativistic angular momentum j in use in the literature (Kozłowski, Jaroszynski & Abramowicz 1978), we have found only minor

²Recall that at low-densities matter will be approximately symmetric and, therefore, $Y_e \simeq 0.5$.

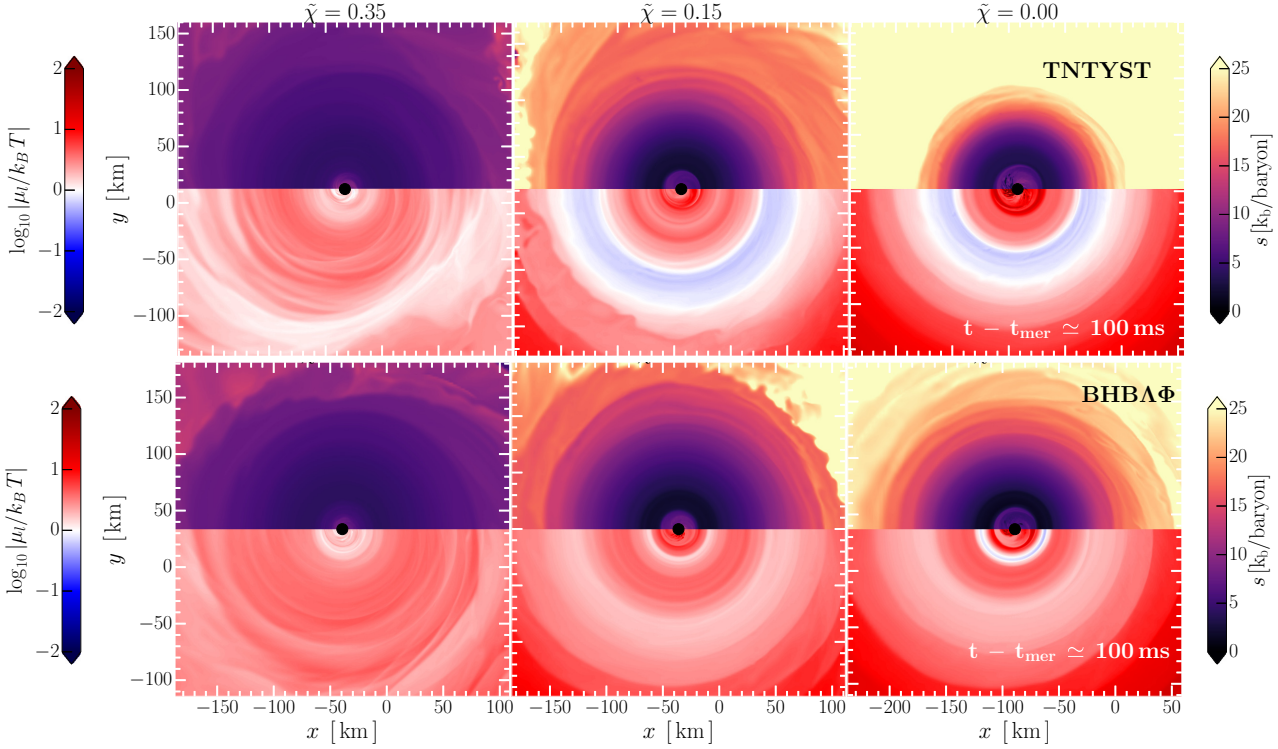


Figure 4. Equatorial view of the entropy s per baryon and the lepton chemical potential μ_1 , relative to the fluid temperature T . The top row shows models computed using the TNTYST EOS, the bottom row $\text{BHBA}\Phi$ models. All results are shown at $\simeq 100$ ms after merger at time t_{mer} .

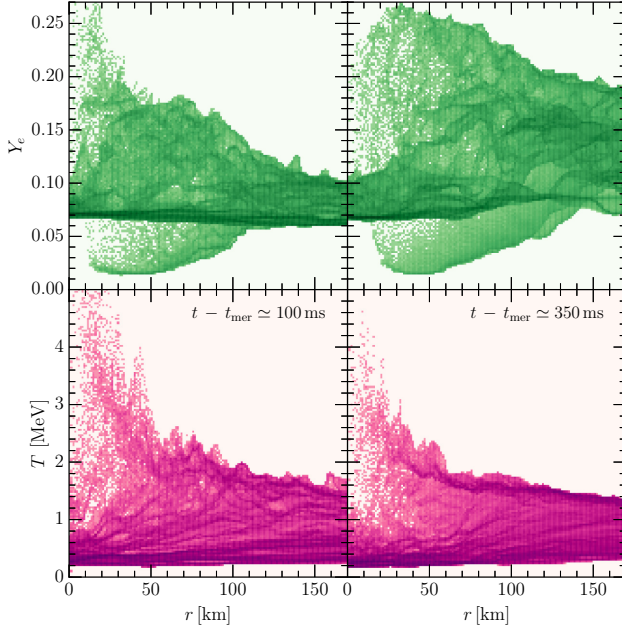


Figure 5. Electron fraction Y_e (top panels) and temperature T (bottom panels) sampled as a function of the cylindrical radius r at two times after the merger. Shown are results for model `TNT.chit.0.35`.

differences between them when extracted from our simulations. For simplicity, we therefore choose to adopt the one used for massive discs $j := hu_\phi$, where h is the specific enthalpy and u_ϕ the covariant azimuthal-component of the fluid four-velocity (Kiuchi et al. 2011). For the highest disc mass and spin (left-hand panel), we find for

large parts of the disc, $\rho > 10^8 \text{ g cm}^{-3}$, that the specific angular momentum is far from being constant, as customarily assumed in simplified models of equilibrium tori. Rather, the specific angular momentum varies in the range $10 < hu_\phi/M_\odot < 20$, and decreases further out at low densities $< 10^8 \text{ g cm}^{-3}$ as required by dynamical stability. Only for lower spins and disc masses, can the specific angular momentum be considered closer to a constant, although also in this case it ranges from $10 < hu_\phi/M_\odot < 15$.

In comparison, Fig. A1 in Appendix A, shows the same distributions but for the mergers using the $\text{BHBA}\Phi$ EOS. While the temperature, entropy, and electron fraction distributions look overall very similar, the angular momentum distributions are different. For high and medium spin (left-hand and middle panel, bottom row), the results do look comparable, but the zero-spin case features a split of the specific angular momentum in two semi-constant branches.

3.3 Magnetic-field evolution

While the disc is cooling, the dynamics of the plasma and magnetic instabilities lead to an increase in the magnetic field strength, as shown in Fig. 7, which displays the evolution of the toroidal and poloidal magnetic energy. Note that after the merger, the disruption of the NS leads to a shearing of the magnetic-field lines in its interior, which causes a sudden amplification of the magnetic field (Rezzolla et al. 2011; Etienne et al. 2012b). Because of the geometry of the disruption event, the amplification will mainly affect the toroidal component of the field. The predominantly poloidal parts of the magnetic fields in the centre of the disrupted star experience a smaller amplification and are mostly accreted by the BH, as can be seen by the sudden drop in poloidal energy directly after merger (left-hand

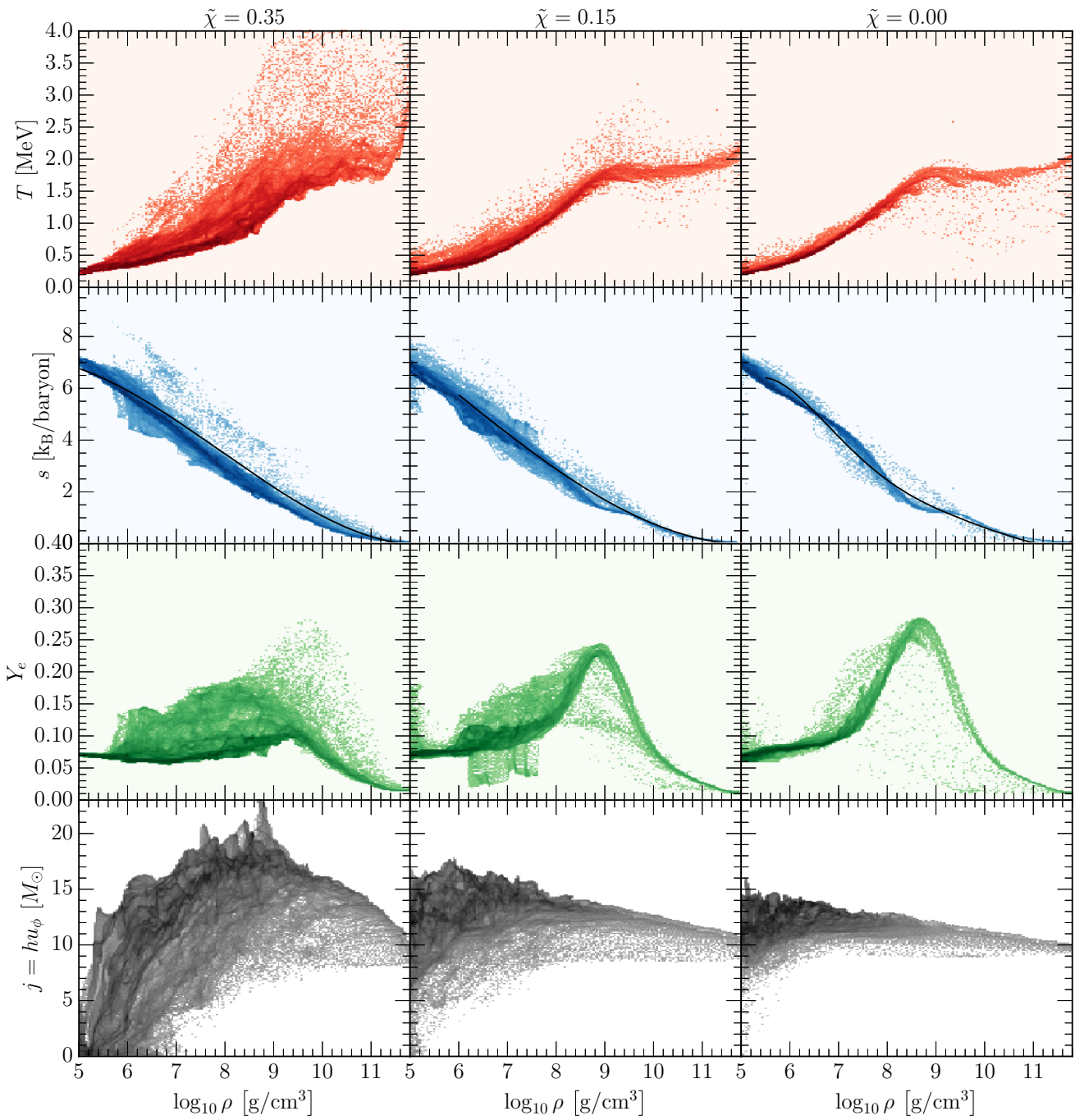


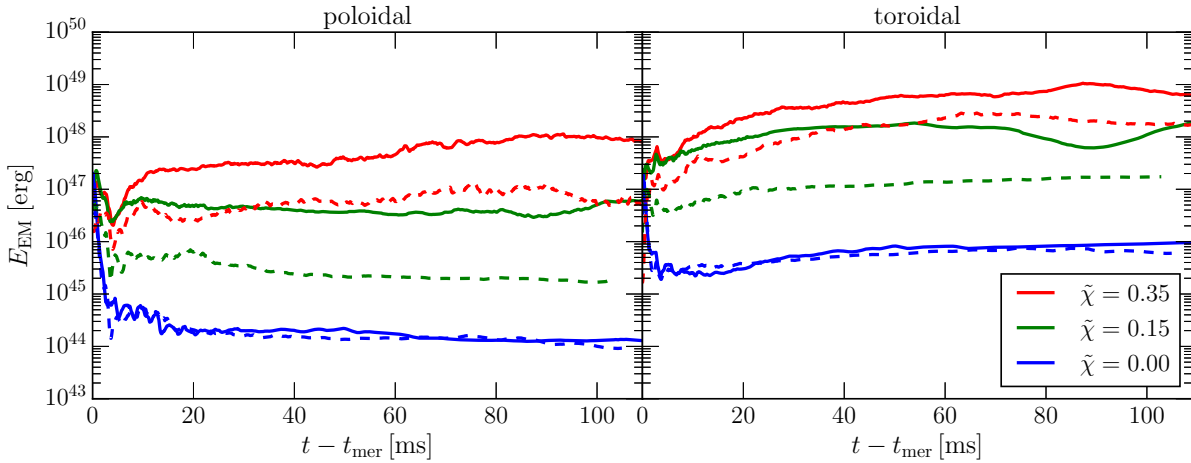
Figure 6. Properties of the accretion discs formed in BH–NS merger simulations using the TNTYST EOS for different effective spins $\tilde{\chi}$ at the same time as in Fig. 2 ($t - t_{\text{mer}} \simeq 100$ ms). Shown are the temperature T , specific entropy per baryon s , electron fraction Y_e , and specific angular momentum $j := hu_\phi$ sampled based on their local rest-mass density ρ .

panel). In the case of the zero-spin binary `TNT.chit.0.00`, almost the entire NS is accreted and only the weakly magnetized matter in the outermost parts of the original NS remain to form the disc. This is accompanied with a very sharp drop in both components of the magnetic energy. After the merger the magnetorotational instability (MRI) (Velikhov 1959; Chandrasekhar 1960; Balbus & Hawley 1991) will begin to drive an early amplification of the magnetic field, which can be seen by an increase in both poloidal and toroidal field components. A key feature to accurately capture this amplification is

with the use of a fourth-order accurate numerical scheme (Most et al. 2019b), which helps us to resolve instabilities, such as the MRI, even at lower resolutions in the outer parts of the disc. The use of such schemes can, however, not alleviate the need for resolving the length scales associated with physical processes and instabilities. Indeed, we find that the lowest mass disc, case `TNT.chit.0.00`, leads to a disc of roughly half the size of the other cases, pointing to the need for higher resolutions than we currently employ. The absence of poloidal field growth for this case confirms that the MRI wavelength

Table 2. Numerical coefficients for the fits of the specific entropy s and magnetic-field strengths $B_{\text{P,T}}$. See equations (5) and (6) for details.

	c_0	c_1	c_2	c_3	c_4	c_5	n_{P}	n_{T}
TNT.chit.0.00	-2.86582187×10^2	1.81083785×10^2	-4.324920×10^1	5.01361071	-2.853×10^{-1}	6.406804×10^{-3}	0.63	0.81
TNT.chit.0.15	1.31709775×10^1	$-5.15110841 \times 10^{-1}$	$-1.91936445 \times 10^{-1}$	$1.19396867 \times 10^{-2}$	–	–	0.60	0.83
TNT.chit.0.35	1.26609813	3.5028831	$-6.0868273 \times 10^{-1}$	2.564125×10^{-2}	–	–	0.68	0.81
BHB.chit.0.00	-2.20695034×10^2	1.44382904×10^2	-3.52546974×10^1	4.16619568	$-2.41611251 \times 10^{-1}$	$5.52949675 \times 10^{-3}$	0.67	0.87
BHB.chit.0.15	2.20750408×10^1	-3.15903230	$6.72177833 \times 10^{-2}$	$3.54576634 \times 10^{-3}$	–	–	0.77	0.97
BHB.chit.0.35	8.39396035	1.38819864	$-4.1548535 \times 10^{-1}$	2.02858×10^{-2}	–	–	0.67	0.87

**Figure 7.** Evolution of the magnetic energy, E_{EM} , after the merger at time t_{mer} . Shown are the total poloidal (left-hand panel) and toroidal component (right-hand panel). The colours refer to the different models in terms of their effective spins, $\tilde{\chi}$. Solid lines represent simulations with the TNTYST and dashed lines with the BHBA- Φ EOSs.

is not fully resolved in large parts of the disc and that the MRI is likely not active in this simulation. Given the low mass of the disc and the low observational prospects, we choose to not repeat this calculation at higher resolution.

Comparing the evolution of the magnetic energy for different BH spins, we find that the high-spin cases feature larger magnetic energies, with the models with the TNTYST EOS (solid curves), having up to an order of magnitude higher electromagnetic energies than the BHBA- Φ models (dashed curves). This already points to a mild EOS dependence on the subsequent disc evolution. Moreover, we can already anticipate that the magnetic-field geometry is largely toroidal by comparing the left-hand and right-hand panels in Fig. 7. Since the initial structure of the field geometry might critically affect the time-scales of the late-time evolution of the disc (Christie et al. 2019), we next present a detailed analysis of the magnetic-field topology.

3.4 Magnetic-field topology

We can further investigate the structure and properties of the magnetic field by looking at density distributions of the poloidal B_{P} and toroidal B_{T} magnetic-field components, as shown in Fig. 8 for the simulations using the TNTYST EOS. Starting from the irrotational case, $\tilde{\chi} = 0.00$ (left-hand column), we can see that, overall, the bulk of the poloidal and toroidal fields follows a power-law dependence with the rest-mass density

$$\log_{10}[B_{\text{P,T}}/\text{G}] = n_{\text{P,T}} \log_{10}[\rho/(\text{g cm}^{-3})] + \text{const.}, \quad (6)$$

where the values of the two coefficients $n_{\text{P,T}}$ are reported in Table 2.

Note that the toroidal magnetic field peaks at 10^{14} G . The poloidal to toroidal ratio is $B_{\text{P}}/B_{\text{T}} \simeq 0.1$, and increases locally to $B_{\text{P}}/B_{\text{T}} \lesssim 10$ for low rest-mass densities $\rho < 10^7 \text{ g cm}^{-3}$. This is mainly due to the appearance of the MRI, which causes a sustained replenishing of the poloidal field (Sadowski et al. 2015). Conversely, this also confirms our initial conclusion that the MRI is likely not resolved in the least massive and, hence, smallest of the discs. While this clearly indicates that any subsequent evolution of this disc at current resolution is not feasible, it also allows us to draw an important conclusion about the correct initial conditions for the magnetic field. Namely, that the profiles seen in the third column of Fig. 8 should be indicative for realistic initial magnetic-field topologies in discs formed directly in BH-NS mergers. Since the subsequent magnetic-field evolution is very modest, these distributions represent the initial magnetic-field configuration in the disc as soon as it equilibrates after merger. More importantly, these distributions are rather different from those normally employed in simulations starting from axisymmetric tori in equilibrium, which often even ignore the presence of a toroidal component.

This qualitative behaviour described before is the same for all discs. However, the larger poloidal-toroidal ratio is indicative of the fact that the MRI is active in increasingly larger parts – and at higher densities – of the discs. For the high-spin case, $\tilde{\chi} = 0.35$, we can clearly see that the MRI is active throughout the disc and that both poloidal and toroidal field grow beyond the simple power-law behaviour outlined before. Looking at the corresponding Fig. A2 in

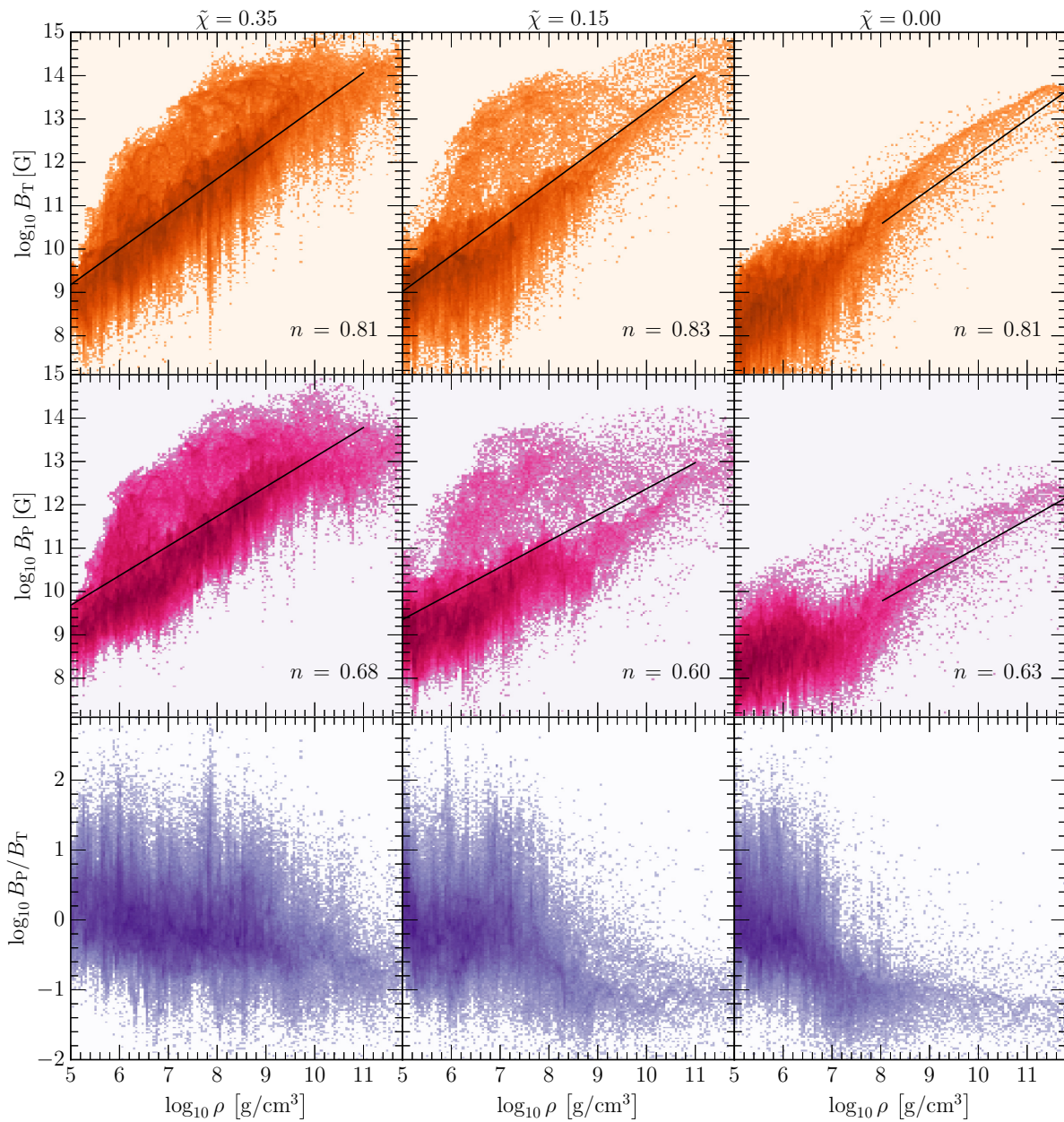


Figure 8. Density-dependent distributions of the poloidal, B_p , and toroidal, B_t , components of the magnetic field at the same time as in Fig. 2 ($t - t_{\text{mer}} \simeq 100$ ms). The simulations shown use the TNTYST EOS and n is defined in equation (6).

Appendix A, it is possible to deduce that this behaviour holds also for a different EOS, and that the overall magnitude of the magnetic field remains insensitive to the initial choice of EOS for the inspiraling NS. None the less, the slope coefficients $n_{p,T}$ are slightly larger when compared to the simulations with the TNTYST EOS. Although this change is rather minor, it does hint that the slightly altered distribution of the magnetic field inside the initial NS is partially imprinted on to the disc, as it would be natural to expect.

3.5 Prospects of jet launching

Having discussed the composition structure of the disc and the magnetic field topology present in the accretion discs formed in (low-mass) BH-NS mergers, we now turn to the prospect of launching a jet

from these systems. While this process has been thoroughly studied for accretion discs found in supermassive BH accretion (Abramowicz & Fragile 2013; Porth et al. 2019; Davis & Tchekhovskoy 2020), only a few attempts have been made in the context of NS mergers, both in ideal (Rezzolla et al. 2011; Kiuchi et al. 2015; Paschalidis et al. 2015; Kawamura et al. 2016; Ruiz et al. 2018b) and resistive MHD (Dionysopoulou, Alic & Rezzolla 2015; Qian, Fendt & Vourellis 2018). Unless an external field was initially seeded by means of a force-free like magnetosphere (Paschalidis et al. 2015; Ruiz et al. 2020), most simulations have only observed the formation of a helical magnetic-field structure in the funnel region (Kawamura et al. 2016), however, not an actual (relativistic) outflow. In most cases, strong baryon pollution from the disc created large ram pressures preventing the funnel from clearing and attaining a magnetically

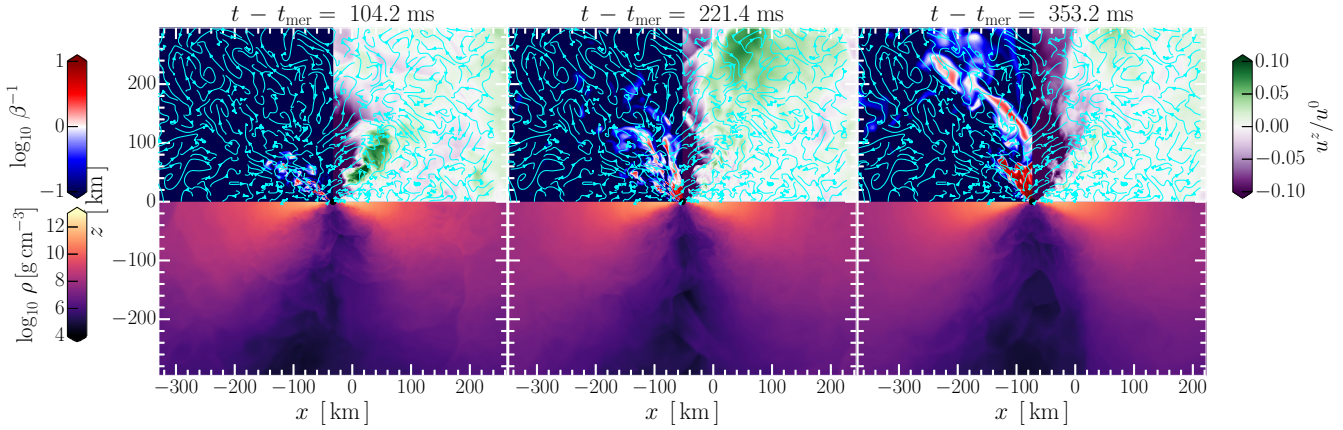


Figure 9. Long-term evolution of the TNTYST.chi.035 system. The top half shows the vertical flow velocity u^z/u^0 and the inverse plasma parameter $\beta^{-1} := b^2/(2p)$, computed in terms of the comoving magnetic energy density b^2 and of the fluid pressure p . The lower half of the panel shows the rest-mass density ρ . The magnetization of the funnel is steadily growing over time (red regions), while the matter inside the funnel is increasingly inflowing (violet regions), indicating potential funnel clearing on longer time-scales.

dominated, force-free state (Kiuchi et al. 2014, 2015). Since most of these simulations were run with low resolutions and for short time-scales $\lesssim 100$ ms, it currently remains an open problem to understand under what conditions the magnetization in the funnel would grow over longer time-scales. Recent simulations of accretion discs with toroidal magnetic fields indeed indicated that the time-scale for magnetic-field growth is significantly longer than for initial poloidal geometries typically used to study jet launching (Christie et al. 2019; Liska, Tchekhovskoy & Quataert 2020). While these studies benefit from having higher resolutions close to the BH horizon, due to the use of better suited spherical coordinate systems, the use of a fully fourth-order numerical scheme allows us to accurately capture magnetic instabilities in the disc with fewer grid points than needed for second-order codes (Most et al. 2019b). Therefore, we evolve one of the systems TNTYST.chi.035 until ~ 350 ms in order to gauge its prospect for jet launching. Since the BH retains a net linear momentum after merger, we continue to solve the Einstein equations alongside those of GRMHD.

In Fig. 9 we report the evolution of the funnel region in terms of plasma parameter $\beta^{-1} := b^2/(2p)$ – where b^2 is the comoving magnetic energy density and p the fluid pressure – and the vertical flow velocity u^z/u^0 . Note that while the funnel starts out being only weakly magnetized (left-hand panel), the magnetization grows steadily over time with increasingly larger portions exhibiting $\beta^{-1} > 1$ (middle and right-hand panels) in the polar regions above the BH (funnel). The projected magnetic-field lines indicate a twistor shape field geometry as observed previously by Kawamura et al. (2016). At the same time, the funnel regions begins to evacuate on essentially the same time-scale. A steadily increasing inflow, indicated by the dark violet regions in Fig. 9, strongly hints to an eventual clearing of the funnel, although large patches are still strongly polluted by disc inflows (lower half of the panels). In order to better quantify the growing magnetization of the funnel, we introduce a characteristic scale-height $\langle z \rangle_{\beta=1}$, which corresponds to the average z -coordinate with the plasma parameter $\beta = 1$. This parameter may be interpreted as a proxy for how the magnetization of the funnel varies in the vertical direction. We caution that a fully force-free funnel would require $\beta \ll 1$, although such values will in practice not be present until shortly before jet launching. We show the corresponding evolution of the scale-height in Fig. 10. Although

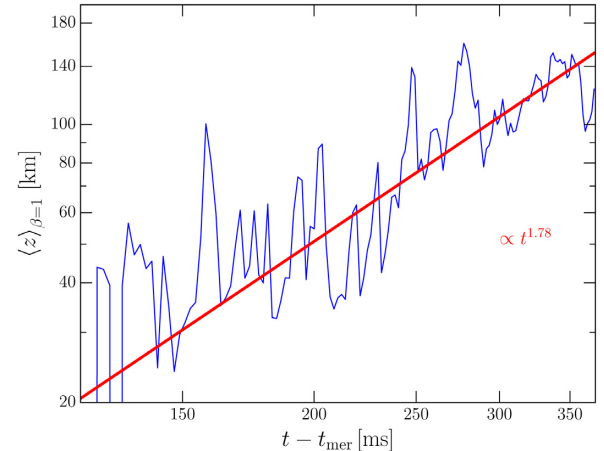


Figure 10. Characteristic scale-height of the magnetized funnel region, where $\langle z \rangle_{\beta=1}$ refers to the average vertical height corresponding to the plasma parameter $\beta^{-1} = b^2/(2p) = 1$. The time is measured relative to the time of merger t_{mer} .

there are inherent fluctuations over time, on average we find that the magnetization scale-height is constantly growing with a power law $\langle z \rangle_{\beta=1} \propto t^\alpha$, with $\alpha = 1.78$. At the end of our simulation, this scale-height extends to about 140 km. If this growth was sustained at the same rate, the scale-height would double around $\simeq 500$ ms. Since the rest-mass densities decrease at larger distances from the BH, it might be possible for this growth to accelerate at sufficient distance from the BH, due to the faster decrease in pressure in those regions.

In order to better understand this behaviour, we have performed a detailed analysis of the magnetic-field topology in the funnel and the disc. To be more precise, we have computed mean magnetic-field energy densities $\langle B^2 \rangle$ for the toroidal and poloidal components in the funnel and in the disc. We define the funnel region simply in terms of density and angular cut-offs. More specifically, we define the funnel to be within 30° from the polar axis and contain densities of at most 10^9 g cm^{-3} . The resulting evolution is shown in Fig. 11. We can see that initially the magnetic-field strength is not growing in the funnel region. Only after $\simeq 200$ ms, when the funnel has begun to

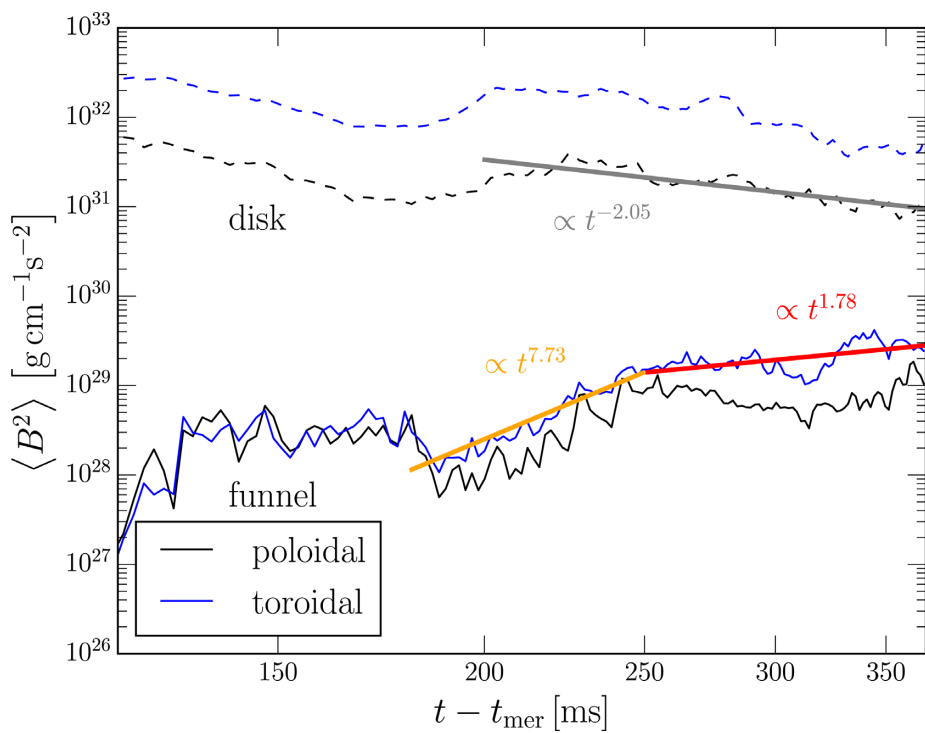


Figure 11. Evolution of the mean magnetic energy density, $\langle B^2 \rangle$, in terms of poloidal (black) and toroidal (blue) components. The evolution is shown separately for the disc (dashed lines) and for the funnel region (solid lines). The time is measured relative to the time of merger t_{mer} .

clear we do see a rapid growth in magnetic energy following a power law with exponent $\alpha \approx 7.73$, which continues for around 50 ms. Afterwards the growth does not stop, but continues at a lower rate. Surprisingly, it turns out that the growth is comparable to the growth of the magnetization scale height, having an exponent $\alpha \approx 1.78$, consistent with the scaling reported in Fig. 10. At the same time the magnetic energy density in the disc is decreasing, likely because of accretion regions with strong magnetic fields in the accretion discs, which are closest to the ISCO, see Fig. 2.

Finally, we also consider the electromagnetic energy outflowing from the system. This is quantified in terms of the Poynting flux

$$\mathcal{L}_{\text{EM}} = \oint T_{i,\text{EM}}^t dS^i, \quad (7)$$

extracted on a spherical surface at around 500 km from the BH. Here $T_{\text{EM}}^{\mu\nu}$ is the electromagnetic part of the stress–energy tensor (Baumgarte & Shapiro 2003). The resulting luminosity is shown in Fig. 12. Starting at $10^{45} \text{ erg s}^{-1}$ at merger, the Poynting flux steadily increases and saturates at $10^{49} \text{ erg s}^{-1}$ after about 300 ms.

4 CONCLUSIONS

We have presented the results of a series of simulations in full general relativity leading to the formation of accretion discs in the aftermath of the merger of BH–NS systems in the near equal-mass regime parametrized by the maximum mass of a non-rotating NS. Including strong magnetic fields, weak interactions, and realistic EOS, the discs have been evolved for $\simeq 100$ ms after merger until a quasi-stationary disc equilibrium has been established. We have then provided a detailed comparison of the disc properties for three different disc masses and BH spins. In particular, we have found that the discs, while remaining very cold, $T \lesssim 2$ MeV, have specific-

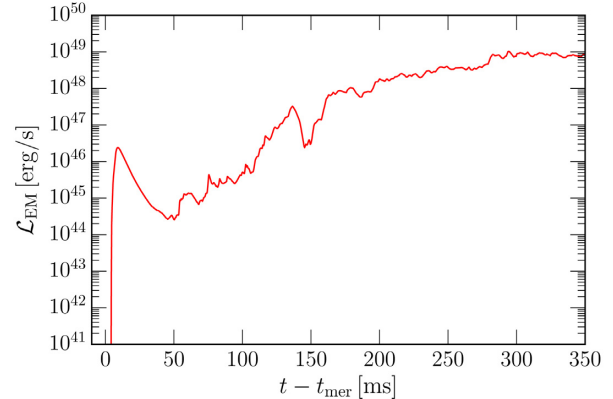


Figure 12. Electromagnetic luminosity \mathcal{L}_{EM} in terms of the Poynting flux for the long-term evolution of model TNTYST.chi .035. The time is measured relative to the time of merger t_{mer} .

entropy distributions that follow power laws in terms of the rest-mass density, $s \propto \rho^{-n}$. Similarly, we were able to confirm that light discs more quickly beta-equilibrate, while more massive discs remain neutron rich (De & Siegel 2020). Importantly, massive discs have specific angular momentum distributions that are far from being constant, as instead customarily assumed in simplified simulations starting from axisymmetric tori in equilibrium, and vary in a rather wide range. At the same time, the specific angular momentum distributions of the lighter discs have smaller ranges of variation and may be roughly approximated as constant.

We have also found that the use of different EOSs with significantly different compactnesses leads to changes in the disc mass, while the other properties of the disc seem to be largely unaffected.

Having performed simulations with strong magnetic fields in the interior of the NS companion, has allowed us to examine the magnetic-field structure present in the post-merger disc when a quasi-stationarity solution is reached. While previous studies have usually superimposed poloidal magnetic fields (Nouri et al. 2018) or – more realistically – toroidal fields (Christie et al. 2019) on post-merger discs, we were able to find density-dependent scaling laws for realistic magnetic-field configurations, i.e. $B \propto \rho^m$. Consistent with previous simulations (Giacomazzo et al. 2011; Rezzolla et al. 2011; Kiuchi et al. 2015) and studies of binary NS mergers (Kiuchi et al. 2014; Kawamura et al. 2016), we find that the field topology is initially strongly toroidal, albeit the onset of the MRI leads to an eventual increase and amplification of the poloidal field.

Although we believe that the results presented in this work will be crucial for future modelling of post-merger accretion discs, some remarks are in order. Owing to the high computational cost of performing BH–NS mergers with accurate descriptions of the microphysics and magnetic-field evolution, we have only investigated the near equal-mass regime. While this might be most indicative for low-mass BH–NS and high-mass NS–NS mergers (see Most et al. 2020c for a comparison), realistic BH–NS mergers are expected to happen for mass ratios $q < 1/4$ (Kruckow et al. 2018). Although disc formation for these systems is largely governed by the spin of the BH (Foucart 2012; Foucart et al. 2018), it remains to be confirmed if the magnetic-field topology and entropy profiles of the disc found here continue to hold also for these systems. Since the primary formation mechanism, i.e. tidal disruption, operates similarly in all cases, we conjecture that most likely our results should be transferable and therefore also hold qualitatively.

Finally, we have investigated the prospects of jet launching from these discs. Although we have not observed the launching of a jet, we did find strong evidence for continued funnel clearing. We have identified the characteristic funnel magnetization and clearing time-scales. In particular we found that the magnetization scale height of the funnel and the magnetic energy associated with it follow a power law, with the dominant component being $\approx t^2$. Interestingly, by the end of our simulation a region extending 140 km above the BH started to reach a strong magnetization as indicated by the plasma beta parameter approaching unity. Finally, we found that a continuous Poynting luminosity of 10^{49} erg s $^{-1}$ is driven at late times.

Future work will be required to further investigate whether jet launching is possible in these systems. Crucially, higher resolutions and longer simulation times > 1 s will be needed. In that context it is of particular relevance to point out that the parameter ranges found for realistic accretion discs in terms of composition, disc mass, specific entropy, and magnetic-field topology can be used to initialize such simulations, thereby removing the need to perform full numerical relativity simulations to accurately study the long-term evolution of this problem.

ACKNOWLEDGEMENTS

ERM thanks Carolyn Raithel for helpful discussions. The authors thank the anonymous referee for useful comments on disc self-regulation. ERM gratefully acknowledges support from a joint fellowship at the Princeton Center for Theoretical Science, the Princeton Gravity Initiative, and the Institute for Advanced Study. The simulations were performed on the national supercomputer HPE Apollo Hawk at the High Performance Computing Center Stuttgart (HLRS) under the grant numbers BBHDISKS and BNS-MIC. The authors gratefully acknowledge the Gauss Centre for Supercomputing e.V. (www.gauss-centre.eu) for funding this project

by providing computing time on the GCS Supercomputer SuperMUC at Leibniz Supercomputing Centre (<http://www.lrz.de>). LR gratefully acknowledges funding from HGS-HIRe for FAIR; the LOEWE-Program in HIC for FAIR; ‘PHAROS’, COST Action CA16214.

DATA AVAILABILITY

Data are available upon reasonable request from the Corresponding Author.

REFERENCES

- Abbott B. P. et al., 2018, *Phys. Rev. Lett.*, 121, 161101
- Abramowicz M. A., Fragile P. C., 2013, *Living Rev. Relat.*, 16, 1
- Alcubierre M., Brügmann B., Diener P., Koppitz M., Pollney D., Seidel E., Takahashi R., 2003, *Phys. Rev. D*, 67, 084023
- Alic D., Bona-Casas C., Bona C., Rezzolla L., Palenzuela C., 2012, *Phys. Rev. D*, 85, 064040
- Anand S. et al., 2021, *Nat. Astron.*, 5, 46
- Annala E., Ecker C., Hoyos C., Jokela N., Fernández D. R., Vuorinen A., 2018, *J. High Energy Phys.*, 2018, 78
- Babiuc-Hamilton M. et al., 2019, *The Einstein Toolkit*, Zenodo, Available at: <https://zenodo.org/record/3522086#.YPk0H0DhWUk>
- Balbus S. A., Hawley J. F., 1991, *ApJ*, 376, 214
- Banik S., Hempel M., Bandyopadhyay D., 2014, *ApJS*, 214, 22
- Baumgarte T. W., Shapiro S. L., 2003, *ApJ*, 585, 921
- Belczynski K., Taam R. E., Rantsiou E., van der Sluys M., 2008, *ApJ*, 682, 474
- Beloborodov A. M., 2003, *ApJ*, 588, 931
- Bernuzzi S., Hilditch D., 2010, *Phys. Rev. D*, 81, 084003
- Bona C., Ledvinka T., Palenzuela C., Zácek M., 2003, *Phys. Rev. D*, 67, 104005
- Caudill M., Cook G. B., Grigsby J. D., Pfeiffer H. P., 2006, *Phys. Rev. D*, 74, 064011
- Chandrasekhar S., 1960, *Proc. Natl. Acad. Sci.*, 46, 253
- Chawla S., Anderson M., Besselman M., Lehner L., Liebling S. L., Motl P. M., Neilsen D., 2010, *Phys. Rev. Lett.*, 105, 111101
- Chen W.-X., Beloborodov A. M., 2007, *ApJ*, 657, 383
- Christie I. M., Lalakos A., Tchekhovskoy A., Fernández R., Foucart F., Quataert E., Kasen D., 2019, *MNRAS*, 490, 4811
- Davis S. W., Tchekhovskoy A., 2020, *ARA&A*, 58, 407
- De S., Siegel D., 2020, preprint ([arXiv:2011.07176](https://arxiv.org/abs/2011.07176))
- De S., Finstad D., Lattimer J. M., Brown D. A., Berger E., Biwer C. M., 2018, *Phys. Rev. Lett.*, 121, 091102
- Deaton M. B. et al., 2013, *ApJ*, 776, 47
- Del Zanna L., Bucciantini N., Londrillo P., 2003, *A&A*, 400, 397
- Del Zanna L., Zanotti O., Bucciantini N., Londrillo P., 2007, *A&A*, 473, 11
- Dionysopoulou K., Alic D., Rezzolla L., 2015, *Phys. Rev. D*, 92, 084064
- Drozda P., Belczynski K., O’Shaughnessy R., Bulik T., Fryer C. L., 2020, preprint ([arXiv:2009.06655](https://arxiv.org/abs/2009.06655))
- Duez M. D., Liu Y. T., Shapiro S. L., Stephens B. C., 2005, *Phys. Rev. D*, 72, 024028
- East W. E., Paschalidis V., Pretorius F., 2015, *ApJ*, 807, L3
- Endrizzi A. et al., 2020, *Eur. Phys. J. A*, 56, 15
- Etienne Z. B., Faber J. A., Liu Y. T., Shapiro S. L., Baumgarte T. W., 2007, *Phys. Rev. D*, 76, 101503
- Etienne Z. B., Faber J. A., Liu Y. T., Shapiro S. L., Taniguchi K., Baumgarte T. W., 2008, *Phys. Rev. D*, 77, 084002
- Etienne Z. B., Liu Y. T., Shapiro S. L., Baumgarte T. W., 2009, *Phys. Rev. D*, 79, 044024
- Etienne Z. B., Liu Y. T., Shapiro S. L., 2010, *Phys. Rev. D*, 82, 084031
- Etienne Z. B., Paschalidis V., Liu Y. T., Shapiro S. L., 2012a, *Phys. Rev. D*, 85, 024013
- Etienne Z. B., Liu Y. T., Paschalidis V., Shapiro S. L., 2012b, *Phys. Rev. D*, 85, 064029
- Etienne Z. B., Paschalidis V., Shapiro S. L., 2012c, *Phys. Rev. D*, 86, 084026

- Etienne Z. B., Paschalidis V., Haas R., Mösta P., Shapiro S. L., 2015, *Class. Quantum Gravity*, 32, 175009
- Fernández R., Metzger B. D., 2013, *MNRAS*, 435, 502
- Fernández R., Quataert E., Schwab J., Kasen D., Rosswog S., 2015, *MNRAS*, 449, 390
- Fernández R., Foucart F., Kasen D., Lippuner J., Desai D., Roberts L. F., 2017, *Class. Quantum Gravity*, 34, 154001
- Fernández R., Tchekhovskoy A., Quataert E., Foucart F., Kasen D., 2019, *MNRAS*, 482, 3373
- Fishbone L. G., Moncrief V., 1976, *ApJ*, 207, 962
- Foucart F. et al., 2013a, *Phys. Rev. D*, 87, 084006
- Foucart F. et al., 2013b, *Phys. Rev. D*, 88, 064017
- Foucart F. et al., 2014, *Phys. Rev. D*, 90, 024026
- Foucart F. et al., 2015, *Phys. Rev. D*, 91, 124021
- Foucart F. et al., 2017, *Class. Quantum Gravity*, 34, 044002
- Foucart F., 2012, *Phys. Rev. D*, 86, 124007
- Foucart F., Duez M. D., Kidder L. E., Teukolsky S. A., 2011, *Phys. Rev. D*, 83, 024005
- Foucart F., Duez M. D., Kidder L. E., Scheel M. A., Szilagyi B., Teukolsky S. A., 2012, *Phys. Rev. D*, 85, 044015
- Foucart F., Hinderer T., Nissanke S., 2018, *Phys. Rev. D*, 98, 081501
- Foucart F., Duez M. D., Kidder L. E., Nissanke S. M., Pfeiffer H. P., Scheel M. A., 2019, *Phys. Rev. D*, 99, 103025
- Fragione G., Loeb A., 2021, *MNRAS*, 503, 2861
- Galeazzi F., Kastaun W., Rezzolla L., Font J. A., 2013, *Phys. Rev. D*, 88, 064009
- Giacomazzo B., Rezzolla L., 2007, *Class. Quantum Gravity*, 24, S235
- Giacomazzo B., Rezzolla L., Baiotti L., 2011, *Phys. Rev. D*, 83, 044014
- Gourgoulhon E., 2012, 3+1 Formalism in General Relativity, vol. 846, Lecture Notes in Physics. Springer Verlag, Berlin
- Grandclément P., 2006, *Phys. Rev. D*, 74, 124002
- Gundlach C., Calabrese G., Hinder I., Martín-García J. M., 2005, *Class. Quantum Gravity*, 22, 3767
- Hayashi K., Kawaguchi K., Kiuchi K., Kyutoku K., Shibata M., 2021, *Phys. Rev. D*, 103, 043007
- Hilditch D., 2013, *Int. J. Mod. Phys. A*, 28, 1340015
- Hinderer T. et al., 2019, *Phys. Rev. D*, 100, 063021
- Kawaguchi K., Kyutoku K., Shibata M., Tanaka M., 2016, *ApJ*, 825, 52
- Kawamura T., Giacomazzo B., Kastaun W., Ciolfi R., Endrizzi A., Baiotti L., Perna R., 2016, *Phys. Rev. D*, 94, 064012
- Kiuchi K., Shibata M., Montero P. J., Font J. A., 2011, *Phys. Rev. Lett.*, 106, 251102
- Kiuchi K., Kyutoku K., Sekiguchi Y., Shibata M., Wada T., 2014, *Phys. Rev. D*, 90, 041502
- Kiuchi K., Sekiguchi Y., Kyutoku K., Shibata M., Taniguchi K., Wada T., 2015, *Phys. Rev. D*, 92, 064034
- Kozłowski M., Jaroszynski M., Abramowicz M. A., 1978, *A&A*, 63, 209
- Kruckow M. U., Tauris T. M., Langer N., Kramer M., Izzard R. G., 2018, *MNRAS*, 481, 1908
- Kyutoku K., Shibata M., Taniguchi K., 2010, *Phys. Rev. D*, 82, 044049
- Kyutoku K., Okawa H., Shibata M., Taniguchi K., 2011, *Phys. Rev. D*, 84, 064018
- Kyutoku K., Ioka K., Shibata M., 2013, *Phys. Rev. D*, 88, 041503
- Kyutoku K., Ioka K., Okawa H., Shibata M., Taniguchi K., 2015, *Phys. Rev. D*, 92, 044028
- Kyutoku K., Kiuchi K., Sekiguchi Y., Shibata M., Taniguchi K., 2018, *Phys. Rev. D*, 97, 023009
- Lackey B. D., Kyutoku K., Shibata M., Brady P. R., Friedman J. L., 2014, *Phys. Rev. D*, 89, 043009
- Lee W. H., Ramirez-Ruiz E., 2002, *ApJ*, 577, 893
- Lee W. H., Ramirez-Ruiz E., 2007, *New J. Phys.*, 9, 17
- Liska M. T. P., Tchekhovskoy A., Quataert E., 2020, *MNRAS*, 494, 3656
- Liu Y. T., Shapiro S. L., Etienne Z. B., Taniguchi K., 2008, *Phys. Rev. D*, 78, 024012
- Löffler F. et al., 2012, *Class. Quantum Gravity*, 29, 115001
- Margalit B., Metzger B. D., 2017, *ApJ*, 850, L19
- Maselli A., Gualtieri L., Ferrari V., 2013, *Phys. Rev. D*, 88, 104040
- Metzger B. D., 2017, *Living Rev. Relat.*, 20, 3
- Most E. R., Weih L. R., Rezzolla L., Schaffner-Bielich J., 2018, *Phys. Rev. Lett.*, 120, 261103
- Most E. R., Papenfort L. J., Dexheimer V., Hanusa M., Schramm S., Stöcker H., Rezzolla L., 2019a, *Phys. Rev. Lett.*, 122, 061101
- Most E. R., Papenfort L. J., Rezzolla L., 2019b, *MNRAS*, 490, 3588
- Most E. R., Papenfort L. J., Tootle S., Rezzolla L., 2021, *ApJ*, 912, 80
- Most E. R., Weih L. R., Rezzolla L., 2020, *MNRAS*, 496, L16
- Most E. R., Papenfort L. J., Weih L. R., Rezzolla L., 2020c, *MNRAS*, 499, L82
- Nathanail A., Most E. R., Rezzolla L., 2021, *ApJ*, 908, L28
- Nouri F. H. et al., 2018, *Phys. Rev. D*, 97, 083014
- Pannarale F., Rezzolla L., Ohme F., Read J. S., 2011a, *Phys. Rev. D*, 84, 104017
- Pannarale F., Tonita A., Rezzolla L., 2011b, *ApJ*, 727, 95
- Papenfort L. J., Tootle S. D., Grandclément P., Most E. R., Rezzolla L., 2021, preprint ([arXiv:2103.09911](https://arxiv.org/abs/2103.09911))
- Paschalidis V., Ruiz M., Shapiro S. L., 2015, *ApJ*, 806, L14
- Perego A., Bernuzzi S., Radice D., 2019, *Eur. Phys. J.*, A55, 124
- Porth O. et al., 2019, *ApJS*, 243, 26
- Qian Q., Fendt C., Vourellis C., 2018, *ApJ*, 859, 28
- Raaijmakers G. et al., 2021, preprint ([arXiv:2102.11569](https://arxiv.org/abs/2102.11569))
- Raithel C. A., Öznel F., Psaltis D., 2018, *ApJ*, 857, L23
- Rezzolla L., Giacomazzo B., Baiotti L., Granot J., Kouveliotou C., Aloy M. A., 2011, *ApJ*, 732, L6
- Rezzolla L., Most E. R., Weih L. R., 2018, *ApJ*, 852, L25
- Rosswog S., Liebendörfer M., 2003, *MNRAS*, 342, 673
- Ruffert M., Janka H.-T., Schaefer G., 1996, *A&A*, 311, 532
- Ruiz M., Shapiro S. L., Tsokaros A., 2018a, *Phys. Rev. D*, 97, 021501
- Ruiz M., Shapiro S. L., Tsokaros A., 2018b, *Phys. Rev. D*, 98, 123017
- Ruiz M., Paschalidis V., Tsokaros A., Shapiro S. L., 2020, *Phys. Rev. D*, 102, 124077
- Schnetter E., Hawley S. H., Hawke I., 2004, *Class. Quantum Gravity*, 21, 1465
- Shibata M., Sekiguchi Y.-I., 2005, *Phys. Rev. D*, 72, 044014
- Shibata M., Taniguchi K., 2008, *Phys. Rev. D*, 77, 084015
- Shibata M., Taniguchi K., 2011, *Living Rev. Relat.*, 14, 6
- Shibata M., Uryū K., 2007, *Class. Quantum Gravity*, 24, S125
- Shibata M., Uryū K., 2006, *Phys. Rev. D*, 74, 121503 (R)
- Shibata M., Zhou E., Kiuchi K., Fujibayashi S., 2019, *Phys. Rev. D*, 100, 023015
- Siegel D. M., Metzger B. D., 2017, *Phys. Rev. Lett.*, 119, 231102
- Siegel D. M., Metzger B. D., 2018, *ApJ*, 858, 52
- Sądowski A., Narayan R., Tchekhovskoy A., Abarca D., Zhu Y., McKinney J. C., 2015, *MNRAS*, 447, 49
- Timmes F. X., Swesty F. D., 2000, *ApJS*, 126, 501
- Togashi H., Nakazato K., Takehara Y., Yamamuro S., Suzuki H., Takano M., 2017, *Nucl. Phys.*, A961, 78
- Velikhov E. P., 1959, Sov. Phys. JETP, 9, 995
- Wan M.-B., 2017, *Phys. Rev. D*, 95, 104013
- Weyhausen A., Bernuzzi S., Hilditch D., 2012, *Phys. Rev. D*, D85, 024038
- Zevin M., Spera M., Berry C. P. L., Kalogera V., 2020, *ApJ*, 899, L1
- Zlochower Y., Baker J. G., Campanelli M., Lousto C. O., 2005, *Phys. Rev. D*, 72, 024021

APPENDIX A: BH_B $\Lambda\Phi$ MODELS

In this appendix, we show the disc properties for models using the BH_B $\Lambda\Phi$ EOS. In particular, Fig. A1 shows the hydrodynamical properties, whereas Fig. A2 shows the topology of the magnetic field present in the disc. These figures should be contrasted with the equivalent representations in Figs 6 and 8, which refer instead to the TNTYST EOS (see Sections 3.2 and 3.3 for a discussion of those results).

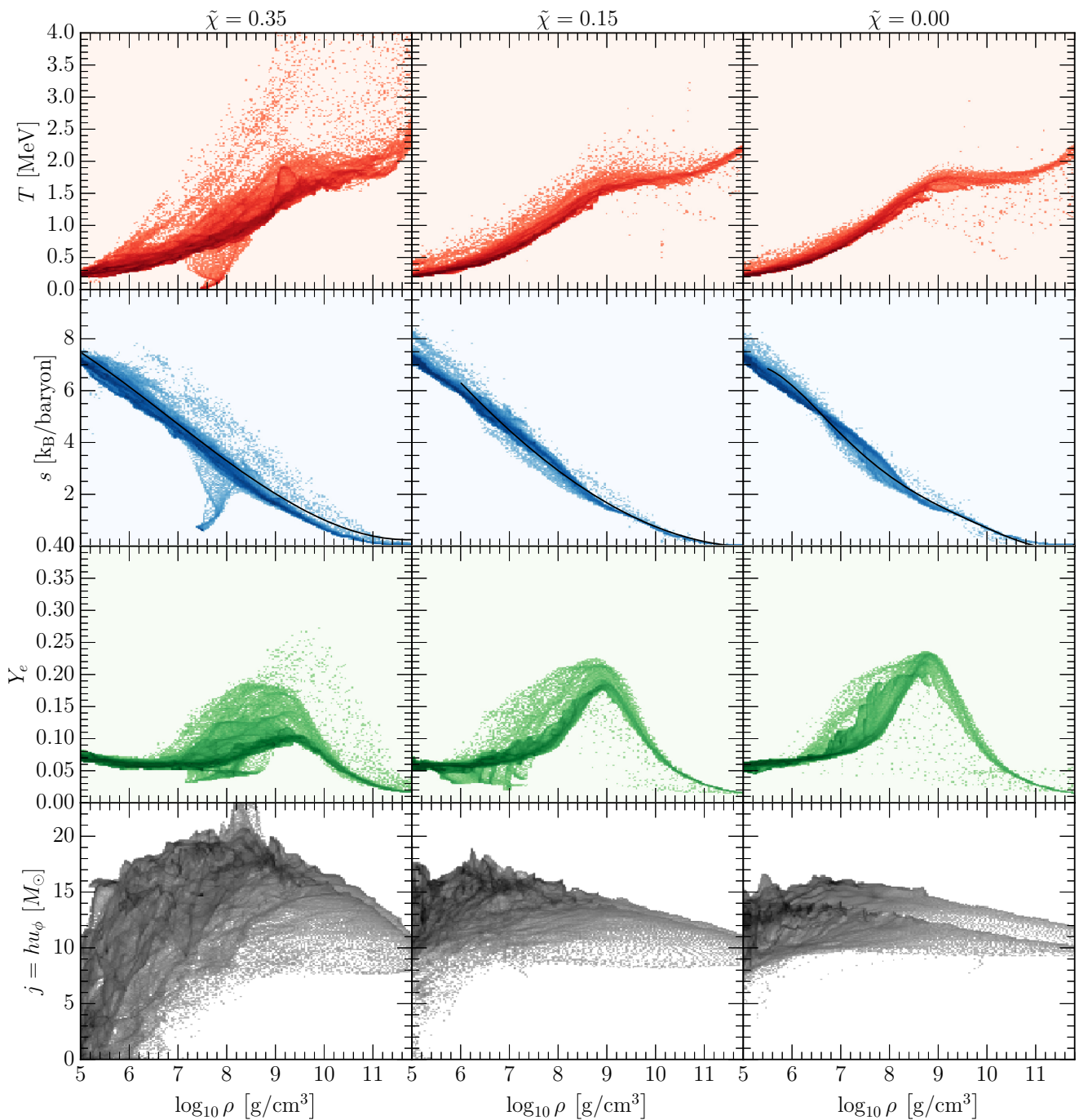


Figure A1. Same as Fig. 6 but for simulations using the $\text{BH}\text{B}\Lambda\Phi$.

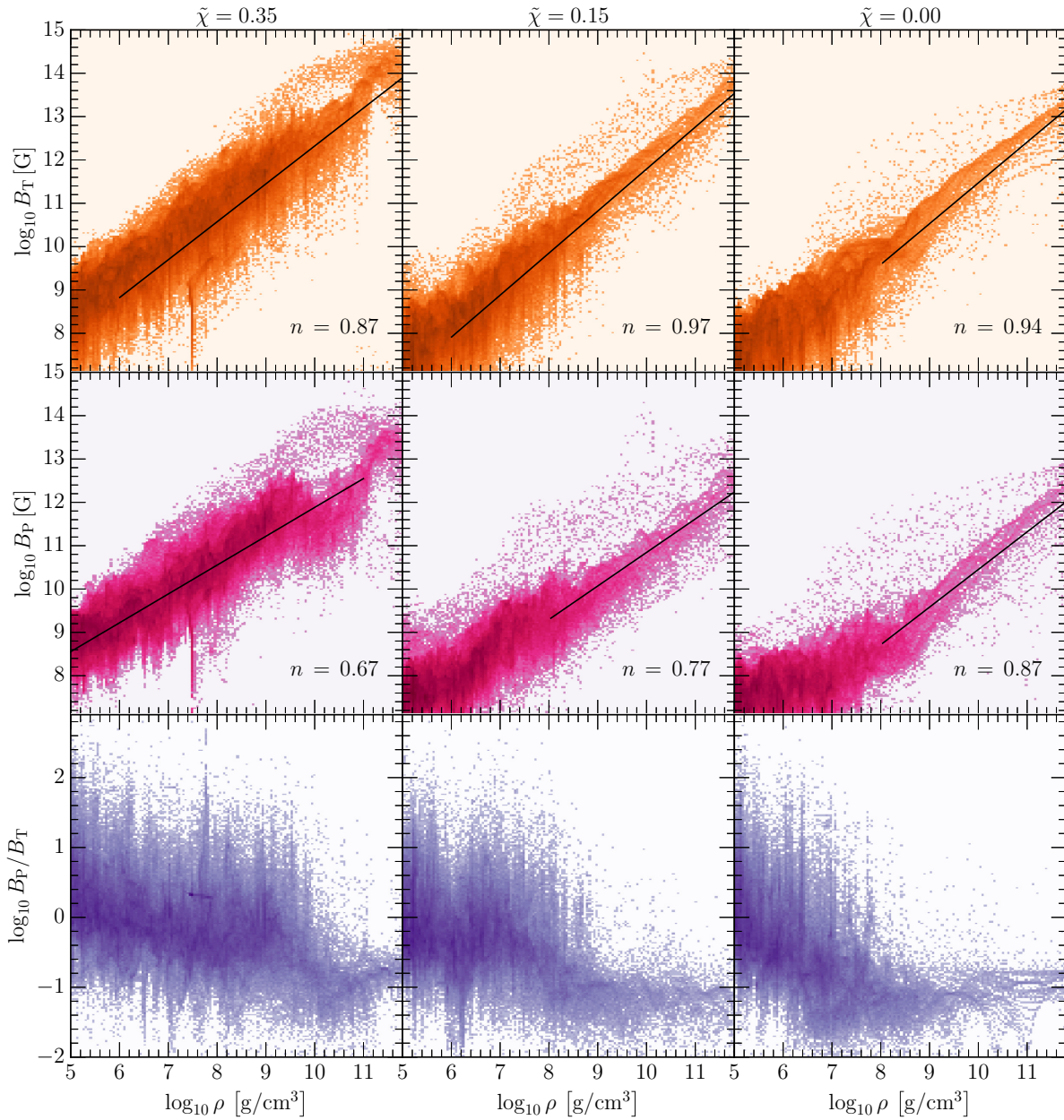


Figure A2. Same as Fig. 8 but using the BHBAΦ EOS.

This paper has been typeset from a $\text{\TeX}/\text{\LaTeX}$ file prepared by the author.